Characterization of the 3-D fracture setting of an unstable rock mass: From surface and seismic investigations to numerical modeling

(Article begins on next page)

13 May 2024

RESEARCH ARTICLE

Key Points:

- The 3-D fracture setting was achieved combining noncontact measures of cliff and fracture geometry, seismic surveys, and numerical modeling
- Active seismic surveys provided valuable constraints on fracture location and persistence within the rock mass
- Passive seismic recordings (seismic noise and earthquakes) highlighted the complex 3-D fracture-driven dynamic response of the site

Correspondence to:
C. Colombero,
chiara.colombero@unito.it

Characterization of the 3-D fracture setting of an unstable rock mass: From surface and seismic investigations to numerical modeling

C. Colombero[1] (ID), L. Baillet[2,3] (ID), C. Comina[1] (ID), D. Jongmans[2,3] (ID), and S. Vinciguerra[1] (ID)

[1]Dipartimento di Scienze della Terra (DST), Università degli Studi di Torino, Turin, Italy, [2]Institut des Sciences de la Terre (ISTerre), Universitè Grenoble Alpes, Grenoble, France, [3]CNRS, Grenoble, France

Abstract The characterization of the fracturing state of a potentially unstable rock cliff is a crucial requirement for stability assessments and mitigation purposes. Classical measurements of fracture location and orientation can however be limited by inaccessible rock exposures. The steep topography and high-rise morphology of these cliffs, together with the widespread presence of fractures, can additionally condition the success of geophysical prospecting on these sites. In order to mitigate these limitations, an innovative approach combining noncontact geomechanical measurements, active and passive seismic surveys, and 3-D numerical modeling is proposed in this work to characterize the 3-D fracture setting of an unstable rock mass, located in NW Italian Alps (Madonna del Sasso, VB). The 3-D fracture geometry was achieved through a combination of field observations and noncontact geomechanical measurements on oriented pictures of the cliff, resulting from a previous laser-scanning and photogrammetric survey. The estimation of fracture persistence within the rock mass was obtained from surface active seismic surveys. Ambient seismic noise and earthquakes recordings were used to assess the fracture control on the site response. Processing of both data sets highlighted the resonance properties of the unstable rock volume decoupling from the stable massif. A finite element 3-D model of the site, including all the retrieved fracture information, enabled both validation and interpretation of the field measurements. The integration of these different methodologies, applied for the first time to a complex 3-D prone-to-fall mass, provided consistent information on the internal fracturing conditions, supplying key parameters for future monitoring purposes and mitigation strategies.

1. Introduction

The behavior of potentially unstable rock cliffs is strongly controlled by the structural discontinuity pattern affecting the rock mass. Persistence, opening, roughness, and orientation of fractures with respect to face topography play indeed a fundamental control on the stability of a jointed rock slope. Classical geological surveys and geotechnical analyses on the accessible cliff faces provide useful information about the structural setting but are limited to outcrop observations and are blind with respect to the inner structure [*Frayssines and Hantz*, 2006]. New advances in both ground-based or airborne remote sensing characterization techniques (tacheometry, photogrammetry, and laser scanning) suffer from the same depth limitations, but can provide a Digital Surface Model (DSM) for fracture analysis even in inaccessible rock exposures [e.g., *Sturzenegger and Stead*, 2009; *Salvini et al.*, 2013]. Particularly, in the last decades, terrestrial remote sensing techniques, including both Terrestrial Laser Scanning (TLS) and Close-Range Photogrammetry (CRP), were proved to be a useful complement to conventional field mapping and rock mass discontinuity characterization [*Coggan et al.*, 2007; *Ferrero et al.*, 2009; *Bistacchi et al.*, 2011; *De Souza et al.*, 2013]. These techniques can potentially allow for indirect geomechanical surveying on steep, high, and dangerous rock faces, in order to retrieve a correct evaluation of fracture location and orientation.

Over the last decades, active and passive seismic methods have been increasingly applied to infer the inner structure of unstable rock masses. Active seismic surveys (e.g., surface refraction and cross-hole tomography) often revealed to be a suitable tool for mapping the physical state and fracturing conditions of unstable bodies. Several successful applications of 2-D and 3-D seismic arrays are reported for the characterization of rockslides with different geological settings and kinematics in the Alps [e.g., *Mauritsch et al.*, 2000; *Jongmans et al.*, 2000; *Méric et al.*, 2005; *Heincke et al.*, 2006; *Colombero et al.*, 2016 and *Valentin et al.*, 2017]. Furthermore, ambient vibration surveys have been recently applied to potentially unstable rock slopes for either investigation or monitoring purposes, showing the capability to detect both reversible and

irreversible modifications within the rock mass that are driven by external factors and controlled by the fracture settings [*Larose et al.,* 2015]. Several previous studies demonstrated that the presence of spectral peaks in the seismic noise measured on prone-to-fall compartments could be associated with their resonance frequencies [e.g., *Lévy et al.,* 2010; *Burjánek et al.,* 2012; *Del Gaudio et al.,* 2013; *Bottelin et al.,* 2013a]. This hypothesis is supported by the absence of similar peaks in the noise spectra recorded on the stable rock mass. Resonance frequency values are expected to be inversely related to the mass and directly related to the stiffness of the unstable volume and of the rock bridges constraining this volume to the stable compartment. In addition, clear spatial directionality was found for the spectral peaks of the resonance frequencies measured on the prone-to-fall compartments. The motion of the first vibration mode revealed to be systematically oriented perpendicularly to the main open fractures separating the unstable sector from the stable rock mass, clearly highlighting the strong fracture control on the stability of these sites. Most of these studies were however limited to the characterization of nearly 2-D fracturing conditions (i.e., unstable volume isolated from the stable massif by a single planar fracture or a set of parallel subvertical discontinuities).

In order to understand the relationships between measured noise directivity and fracture geometry, simplified 3-D numerical modeling has been tentatively carried out in a few case studies. *Lévy et al.* [2010] performed 3-D modal analysis on a prone-to-fall limestone column in the Vercors massif (Chamousset, French Alps). The unstable volume geometry was derived from LIDAR data and one fracture was inserted at the back separating the column from the stable sector. Clamped boundary conditions were set where fresh rock ruptures were observed after the collapse of the block (about 21,000 m^3). The 3-D modal analysis allowed identifying the vibration modes corresponding to the first three resonant frequencies extracted from ambient seismic noise analysis (3, 7, and 20 Hz). The first detected frequency was found to be associated to a flexion mode of the upper part of the column, perpendicular to the rear fracture separating the stable and unstable sectors. The second and third frequencies were referred to a torsion of the column around its vertical axis and a flexion mode along the rear fracture azimuth, respectively. Using a similar approach, *Bottelin et al.* [2013b] investigated 3-D modal and thermal analysis of another limestone column of the Vercors Massif (Les Arches, French Alps) with a potentially unstable volume of about 1000 m^3, delineated by a single open rear fracture. Also in this study, 3-D numerical modeling allowed the reconstruction of the first three vibration modes corresponding to the measured resonance frequencies (6, 7.5, and 9 Hz). Once again, the first mode was attributed to bending of the rock column perpendicular to the rear fracture. In this case, the second and third modes were inverted with respect to *Lévy et al.* [2010] and related to bending parallel to the fracture and torsion around the vertical axis respectively. *Moore et al.* [2011] used seismic noise and earthquake recordings to investigate site effects at the Randa unstable rock slope (Switzerland, around $5 \cdot 10^6$ m^3), finding spectral amplification around 2, 3, and 4.5 Hz. The dynamic behavior of the site was simulated using a discontinuous elastic model. The presence in the model of steeply dipping fractures was found to be crucial for rebuilding the observed site response.

As for the past passive monitoring campaigns, also these previous numerical applications are however always referred to unstable sites with a nearly 2-D geometry. New effort is thus needed toward the comprehension of these phenomena in more complex and full 3-D site conditions. With this aim, *Moore et al.* [2016] measured the resonance frequencies of a natural sandstone arch (Rainbow Bridge, Utah), identifying seven distinct modes of vibration between 1 and 6 Hz, with distinct polarization directions. The 3-D numerical analysis, using a photogrammetric model of the bridge, succeeded in reproducing the measured frequency values and orientations and provided valuable detail on the complete displacement field for each vibration mode.

In order to extend the applicability of the described techniques to a complex 3-D fractured rock mass, a novel approach is presented in this work. A complete characterization of the fracturing state of an unstable rock cliff, with steep topography and complex 3-D fracture settings, is attempted by integrating surface and seismic investigations together with numerical modeling. Particularly, location and orientation of the main fractures were achieved in this study through a combination of field observations and noncontact geomechanical measurements on oriented digital images of the cliff, resulting from a past laser scanning and photogrammetric survey. Once fracture geometry was retrieved, the estimation of fracture persistence within the rock mass was obtained from the processing of surface active seismic surveys. Ambient vibration and earthquakes recordings were then used to assess the fracture control on the site response. All the retrieved information was combined into a finite element 3-D model of the site, which enabled both validation and interpretation of the complex field data set of resonance frequencies and related 3-D orientations.
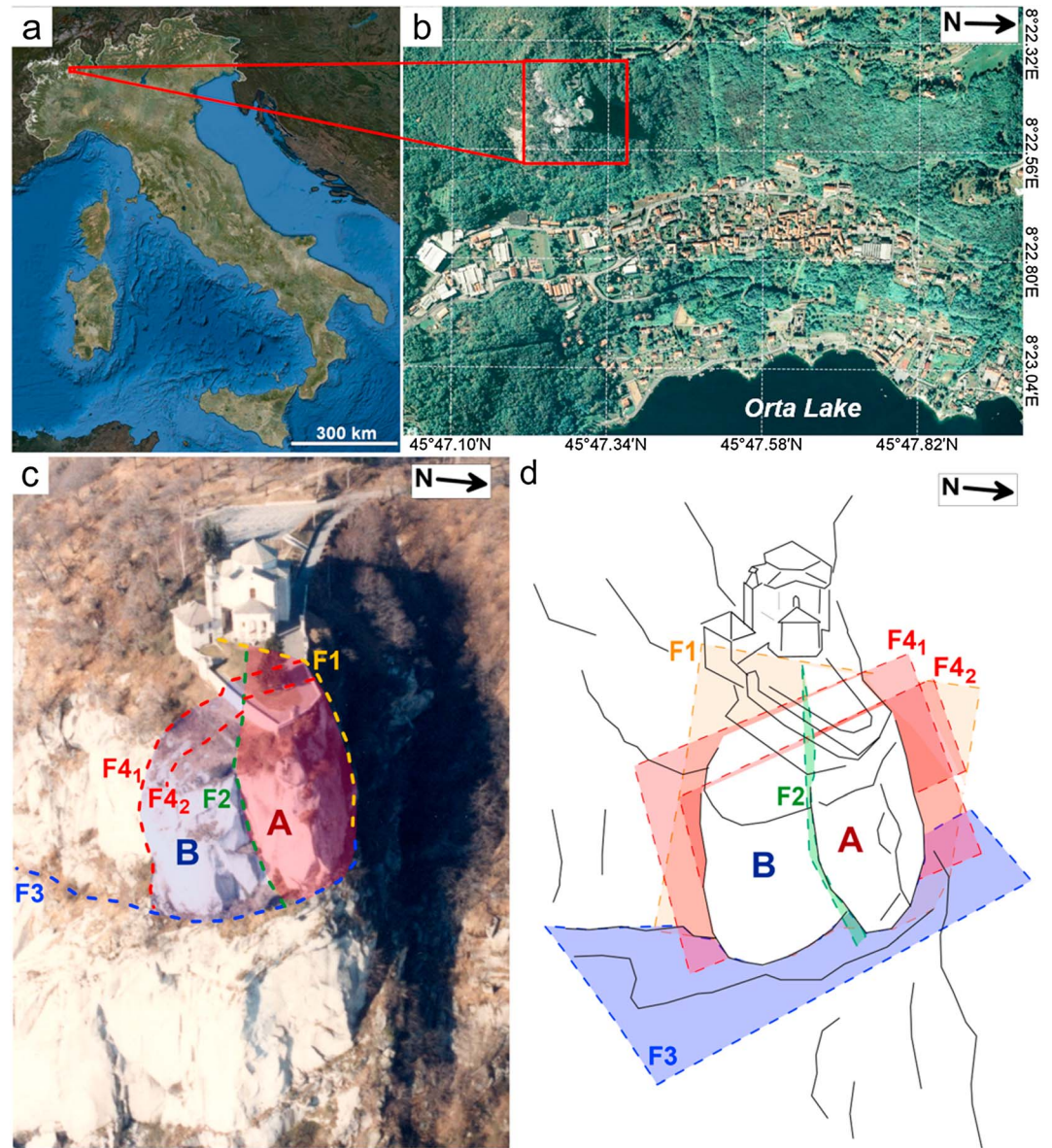
Figure 1. (a) Geographical location of the cliff of Madonna del Sasso (NW Italian Alps). (b) Aerial view of the area. (c) Southern aerial view of the site with traces of the main fractures (from F1 to $F4_{1-2}$) highlighted with colored dashed lines. (d) Simplified sketch of the 3-D fracture planes. In Figures 1c and 1d the two potentially unstable sectors are highlighted with letters A and B.

2. Test Site and Field Observations

The cliff of Madonna del Sasso (45°79′N, 8°37′E) lays on the western shore of the Orta Lake, in northwestern Italian Alps (Figures 1a and 1b). Three vertical sides (north, south, and east faces) of the cliff are directly exposed over the lake surroundings, with a height of approximately 150 m from the lake level. From the geological point of view, the cliff consists entirely of granite (*Granito di Alzo*) and belongs to a larger NE-SW elongated Permian batholith [*Boriani and Giobbi*, 2004]. An eighteenth century church and a suggestive panoramic square are located at the top of the cliff, while several buildings, including houses and small factories and an important road (SP 46) connecting the villages of the western shore of the lake, are placed at the bottom of the slope. The present almost inaccessible steep topography of the site is the result of both the peculiar geostructural background and the intense mining activity lasting until a few decades ago on the free sides of the cliff.

From a structural point of view, a preliminary geomechanical characterization of the site carried out by *Lancellotta et al.* [1991] led to define the rock mass as intact or massive but affected by four main widely spaced joint sets (dip direction/dip, in degrees from N direction and horizontal plane, respectively): K1 (110/75), K2 (0/80), K3 (150/15), and K4 (50/75). At the summit of the cliff, the most open and persistent fractures belonging to each K system (hereafter referred as $F1$, $F2$, $F3$, $F4_1$, and $F4_2$; Figures 1c and 1d) create a complex 3-D pattern of intersections, which tend to isolate two frontal portions of the cliff (sectors A and B), with an estimated total volume of about 12,000 m^3. Particularly, sector A is presumably delimited by fractures $F2$ and $F1$ on the sides, while sector B is bordered by $F2$ and $F4_1$ (the main fracture of the K4 system). Both sectors are truncated at the base by $F3$. Even if the main fractures are easily recognizable in aerial and ground-based pictures of the site, from the panoramic square on the top of the cliff, only $F2$ and $F4_1$ are directly observable. Particularly, along $F4_1$ surface trace, there is a clear evidence of displacement: a decimetric step dislocates the lawn and the confining walls of the panoramic square. The presence of a secondary fracture of the same K4 system ($F4_2$) was already reported in *Lancellotta et al.* [1991], at a distance of approximately 8 m from $F4_1$, toward the lake. Nowadays, no evidences of this fracture are noticeable on the cliff faces or on the panoramic square. Before several maintenance works performed on the site in the last years, fracture $F2$ showed the widest opening (around 50 cm) with a significant persistence within the rock mass and apparently no filling material in the first 10 m depth. Similar observations were made on fracture $F4_1$, particularly in the occasion of isolated phenomena (e.g., in winter 2013 and spring 2015), when several damages and confined collapses occurred in the grassy yard at the top of the cliff. Particularly, during the last critical episode, consequent to intense and long-lasting rainfalls (March–April 2015), an open depth of 12 m was directly measured along $F4_1$ dip direction, in a big open chasm generated in the central part of the panoramic square. Intense upward flows of cool air confirmed the deep persistence and opening of these two fractures, which are supposed to predominantly control the stability of the cliff. Both $F4_1$ and $F2$ surface traces were accurately located with GPS measurements, but the estimation of their mean dip was not possible from the summit of the cliff. Additionally, the other two fractures ($F1$ and $F3$) show surface traces only visible on the high and almost inaccessible vertical faces of the cliff, thus preventing direct observation and measurements.

3. Fracture Location and Orientation: Noncontact Geomechanical Survey

Further efforts were needed for the retrieval of fracture geometry on the high vertical faces of the cliff. Fracture locations and orientations are indeed a basic requirement for both the complete characterization of the unstable compartments and the construction of a realistic 3-D model of the site. With this aim, measurements of fracture surfaces performed with a noncontact procedure are described in this section.

A ground-based laser-scanning survey coupled with the photogrammetric technique was carried out by SIR spin-off company of Politecnico di Torino, in 2011. The survey was undertaken using a Riegl VZ-400 system coupled with a calibrated high-resolution digital camera, from the southeastern base of the cliff. Six scan positions were adopted in order to minimize the presence of dead zones and maximize the coverage, with a sampling step of about 20 mm on the rock surface. Despite this approach, due to the height of the cliff and the limitations caused by the ground-based viewpoints, some areas could not be sampled, especially near the summit yard, the northern face, and around the vegetation-covered ledges. Images from the digital camera resulted in an average Ground Sample Distance (GSD) of 20–30 mm, in the areas described by the high-density cloud. Digital images were used to color the point cloud, obtaining over 30 million points with associated RGB values (Figure 2a). Point cloud alignment and georeferencing were performed using natural and artificial targets placed on the cliff (retroreflective target type) surveyed through a three-dimensional network, measured by integrated topographical and GNSS techniques. An on-purpose digital platform was realized (AdHoc software) for the management of the colored point cloud, the related Digital Surface Model (DSM), and the oriented photos. Specific tools were integrated in the software for the measurement of planar orientations (Figures 2b–2d). In this way, several measurements on the surfaces limiting the main fractures were possible.

The average orientation of each discontinuity set was extracted by density contouring of the poles to the 92 measured planes on the stereogram shown in Figure 3a. Stereographic projections of the extracted representative great circles are reported in Figure 3b, in comparison with the orientations estimated by
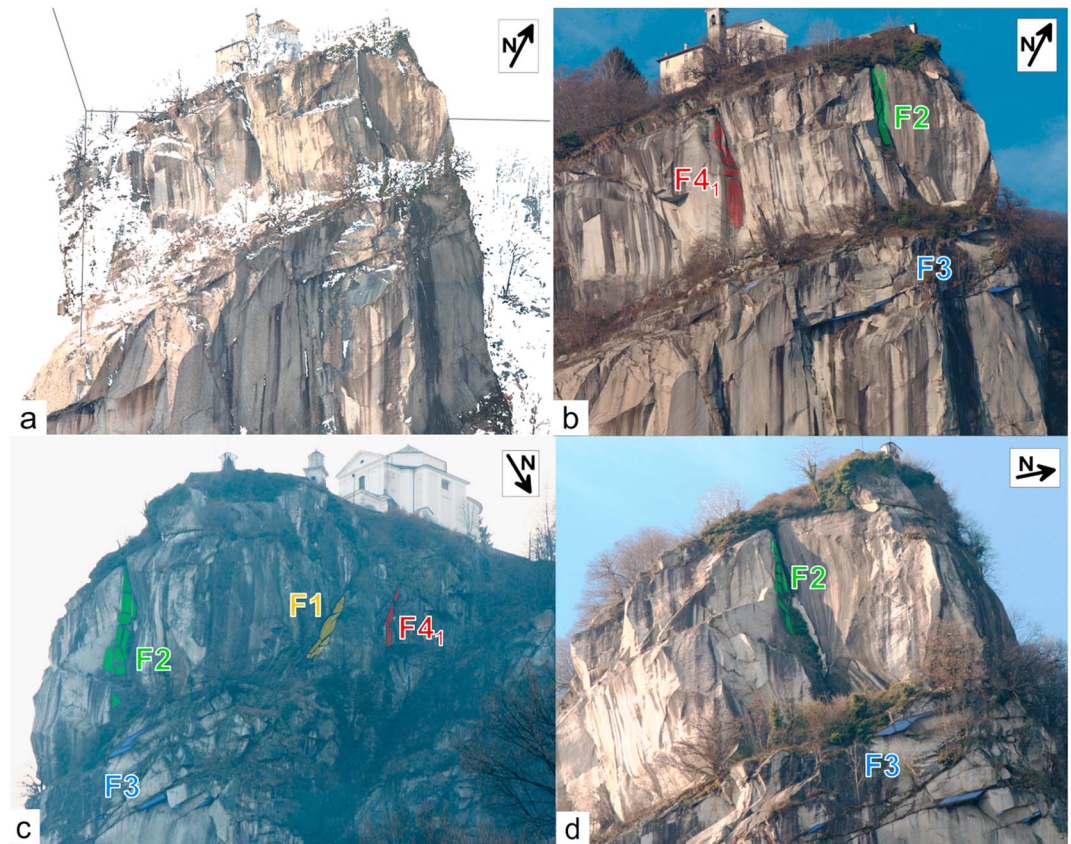
Figure 2. (a) Colored point cloud of the cliff of Madonna del Sasso obtained from the combined laser scanning and photogrammetric survey, view from south. (b–d) Examples of oriented pictures enabling measurements of the fracture planes (colored polygons) in AdHoc software: (b) view of the south, (c) north, and (d) east faces of the cliff.

Lancellotta et al. [1991]. While the obtained dip directions are in perfect agreement with the previous study, the dip angle is found to be lower for F1 ($-10°$) and slightly higher for F4$_1$ ($+5°$). These differences with respect to previous assessments revealed the importance of the TSL and CRP tools in overcoming the difficulties imposed by the steep topography for the construction of a reliable 3-D fracture geometry.

4. Fracture Location and Depth: Active Seismic Surveys

Since field and noncontact observations only supplied an exterior knowledge of the fracturing conditions, an interior characterization, provided by geophysical investigations, was needed. Seismic data acquired on site are analyzed in this section with the aim of confirming fracture locations and evaluating the related persistence within the rock mass, with the help of 2-D numerical modeling.

4.1. Field Data

The areal coverage and depth of investigation of the geophysical surveys performed at the site were intensely limited by its steep topography and high-rise morphology. Even if the summit of the cliff is easily accessible, the limited available space, approximately 35 m × 20 m, does not allow the deployment of long arrays. Obtaining a depth of investigation enabling to reach the basal fracture F3 (approximately at 45 m depth from the cliff summit) is thus impossible. Moreover, the sharp and complex morphology of the site, along with the highly fractured medium, can cause strong scattering and attenuation of seismic waves.

Despite the mentioned limitations, an extensive geophysical campaign was undertaken at the site in 2013–2014. Seismic cross-hole tomographic results, reported in *Colombero et al.* [2016], succeeded in roughly defining the presence of F4$_1$ and F4$_2$ beneath the yard at the top the cliff, but with a poor spatial resolution imposed by the survey geometry and the high attenuation and scattering within the fractured medium, thus preventing accurate fracture imaging and persistence evaluation.
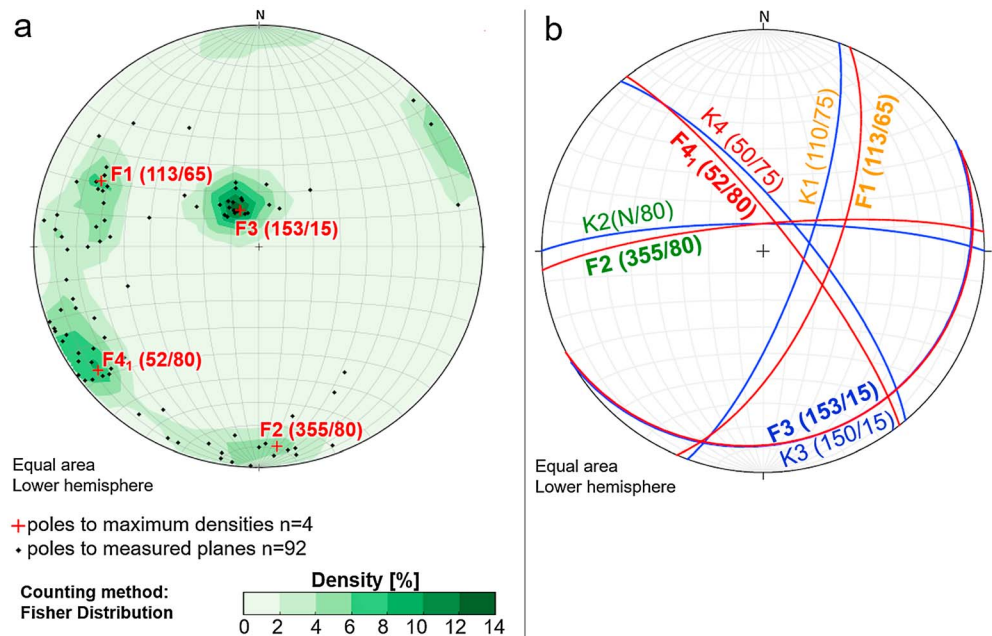
Figure 3. (a) Density contours on the planar measurements obtained from the noncontact survey. Poles to the measured planes are plotted with black dots, the mean orientation for each measured fracture is shown with the red cross. (b) Comparison between the noncontact resulting mean orientations, in red, and the mean orientations of the fracture systems reported in *Lancellotta et al.* [1991], in blue. Fracture orientations are reported in brackets as dip direction/dip (in degrees from N direction and horizontal plane, respectively).

However, simple observations on the raw surface seismograms and related spectral content may provide a fast and clear tool to confirm fracture location, as already demonstrated by several authors on real-scale prospecting data [e.g., *Bottelin et al.,* 2015] or by numerical investigations [e.g., *Li and Vidale*, 1996]. In the current study, a surface seismic survey acquired on the yard at the top of the cliff was therefore used to evaluate the potentiality of detecting fracture presence and estimating the related open depth. The analyzed seismic line was acquired along the longitudinal section of the panoramic square, using 48 vertical geophones (4.5 Hz) with a spacing of 0.75 m (Figure 4a). A sledge hammer impacting on a metallic slab was used as seismic source. Several shots were performed at both ends and seven locations along the line. For each shot, signals were recorded for a total length of 512 ms and a sampling interval of 31.2 μs. The seismic line perpendicularly intersects the decimetric displacement step related to the presence of $F4_1$, between geophones G28 and G29. Furthermore, from the measurements of *Lancellotta et al.* [1991] and from the cross-hole refraction tomographic results reported in *Colombero et al.* [2016], the minor fracture $F4_2$ is expected to cross the line, around G18–G19. Interferences with F1 and F2 are also possible toward the end of the line, in proximity of the church building, from G45 to G48.

The amplitude-normalized seismograms related to sources placed at both ends of the profile (direct shot: −1 m from G1 and reverse shot: +1 m from G48) are shown in Figures 4b and 4c, respectively. Significant changes in the waveforms are detected along the surveyed line. The main perturbations of the wavefield are located around G28–G29, in correspondence of the surficial $F4_1$ displacement step, and around G18–G19, where $F4_2$ is expected at depth. Close to both fracture locations, the duration of the traces visibly increases. Additionally, a clear change in the dominant frequency content of the traces located before (50–60 Hz) and after (>100 Hz) $F4_1$ is particularly visible on the direct seismogram (Figure 4b). Only high-frequency acoustic waves seem therefore to survive in the propagation after $F4_1$. These rapid changes in wave shape and frequency are characteristic of heterogeneous and fractured media that generate scattering [*Levshin et al.,* 1989]. A marked backward reflection is also noticeable in these last traces of the same seismogram. On the reverse shot (Figure 4c), a minor change in the waveforms is detected as well around G45. Since, these anomalies are located close to the limit of the line and can be related to the interference with the buildings, the effects of fracture F1 (or F2) could not be further deepened.
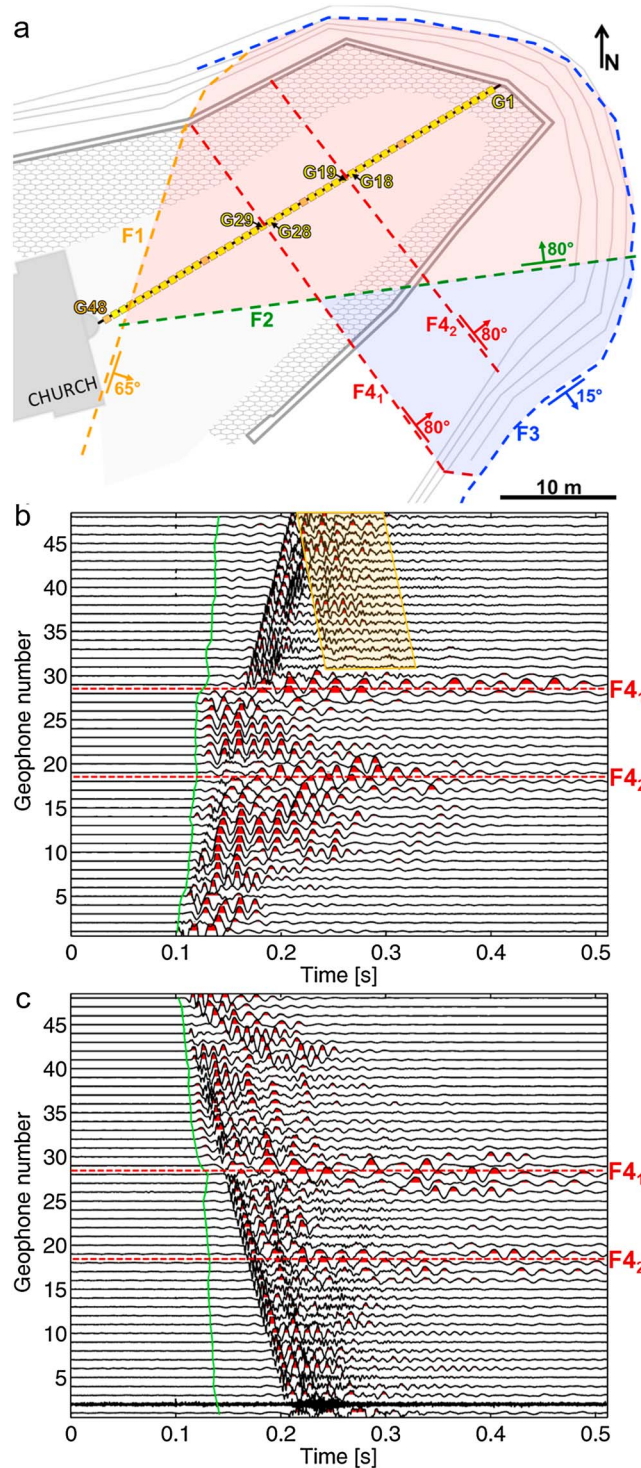
Figure 4. (a) Schematic map of the site with location of the active seismic line, geophone G1 is located at the edge of the cliff (toward the lake) while G48 is the closest to the church. The two fractures are approximately located between G28-G29 ($F4_1$) and G18-G19 ($F4_2$). Seismograms for seismic source located (b) at −1 m from G1 (direct shot) and (c) at +1 m from G48 (reverse shot). Fracture approximated locations are highlighted with the red dashed lines. In the seismograms, the green line marks first-arrival-time picking. In Figure 4b, the yellow polygon highlights the backward reflection at the end of the profile.

To confirm fracture presence and location, the energy content of the two seismograms was computed from the squared amplitude of each trace, after recovering geometrical spreading (Figure 5a). Clear energy concentrations, followed by sudden energy decays, are found in correspondence of the two supposed fracture locations. This can be due to the fact that part of the energy of the direct wave train is reflected back and does not propagate further over the fractures, as already observed in *Bergamo and Socco* [2014] and *Hyslop and Stewart* [2015].

As for the raw seismograms and the energy distribution, also the frequency content of the traces exhibited significant modifications in wave propagation, occurring not only at fracture locations and likely due to the heterogeneity of the medium. In Figures 5b and 5c the Fourier spectra of the direct and reverse shots, normalized to the maximum of the trace closest to the source, are shown in logarithmic color scale. For the direct shot (Figure 5b) an abrupt fall in the spectral amplitude of the seismic traces is detected after $F4_1$, while perturbations due to $F4_2$ seem more restrained. The same clear drop can be found on the reverse shot (Figure 5c) at $F4_1$ location, followed by a weak concentration in spectral amplitude in correspondence of $F4_2$. These results confirm that the deepest and most persistent fracture of K4 system affecting the site is $F4_1$, while the influence of $F4_2$ appears less significant.

In order to retrieve $F4_1$ and $F4_2$ persistence within the rock mass, processing of the surface wave content (Rayleigh waves) was undertaken. The adopted method for fracture depth estimation, described in *Hévin et al.* [1998] and successfully tested in *Bièvre et al.* [2012], is based on the spectral content of the recorded seismic traces. Since the depth of penetration of Rayleigh waves increases as their frequency decreases, only low frequencies of the incident wave are expected to have enough energy below the fracture to be
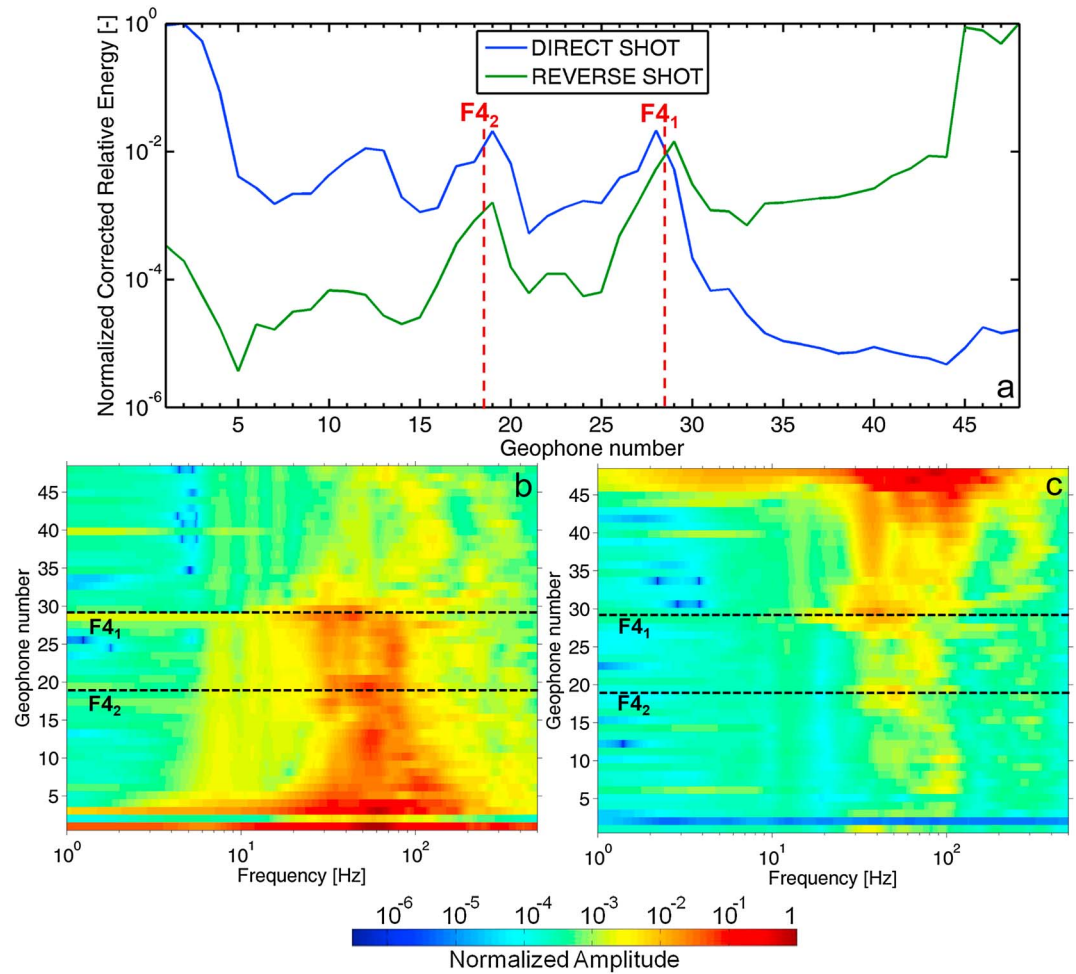
Figure 5. (a) Normalized energy content computed for the direct (in blue) and reverse (in green) shots after correcting for geometrical spreading. Fourier spectra of the raw traces normalized to the maximum of the trace closest to the source, (b) for the direct shot and (c) for the reverse shot. $F4_1$ and $F4_2$ locations are highlighted with dashed lines in each plot.

transmitted. From the spectral ratio of the transmitted over the incident waves, a cutoff frequency (f) can be therefore determined, which can be directly linked to the fracture depth (z). Considering the maximum energy of a Rayleigh wave propagating around a depth of approximately one third of its wavelength (λ), as experimentally and numerically demonstrated in *Hévin et al.* [1998], the fracture depth can be roughly estimated from

$$z = \frac{\lambda}{3} = \frac{v_R}{3\,f} \tag{1}$$

where V_R is Rayleigh wave velocity.

Spectral ratios across $F4_1$ and $F4_2$ were calculated using parts of the direct seismogram showing a quite homogeneous wavefield, considering pairs of traces respectively located after (T) and before (I) the fractures:

$$\text{Spectral Ratio}_{T/I} = \frac{Y_T(f)}{Y_I(f)} \tag{2}$$

where $Y(f)$ is the discrete Fourier transform of traces T = G34, …, G44 and I = G23, …, G26 across $F4_1$ or T = G23, …, G26 and I = G6, …, G13 across $F4_2$.

Resulting T/I spectral ratios are shown in Figures 6a and 6b. Comparing the results across the two fractures, T/I curves exhibited different shapes and positions of the minima (m1 and m2) which can be considered as the
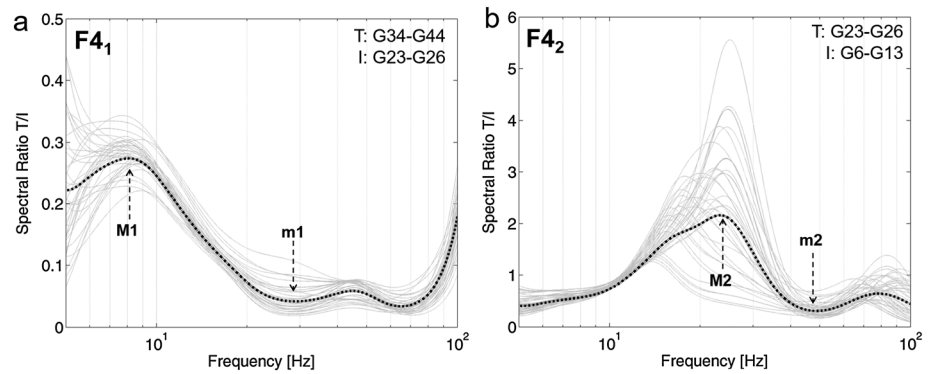
Figure 6. Transmitted-over-incident-wave (T/I) spectral ratios across (a) $F4_1$ and (b) $F4_2$ computed on the direct shot. Gray curves refer to the spectral ratios of each couple of transmitted and incident recording geophones, the black bold dashed line is the mean computed over all the considered couples. Arrows highlight the positions of the minima (m) and maxima (M) in the average spectral ratios, for further comparison with numerical results.

cutoff frequencies related to the fracture depths. Particularly, a significant drop in the *T/I* spectral ratio is found at an average cutoff frequency of 28 Hz for $F4_1$ (*m*1, in Figure 6a) and at higher frequencies, around 46 Hz, for $F4_2$ (*m*2, in Figure 6b), thus confirming again that $F4_1$ is deeper than $F4_2$. The position of the spectral ratio maxima has been also determined ($M1 = 8$ Hz for $F4_1$ and $M2 = 23$ Hz for $F4_2$) for further comparison with numerical results (section 4.2).

Unfortunately, attempts to extract a representative dispersion curve from the surface survey did not provide stable results, even trying to use reduced and homogeneous parts of the seismograms. However, using an average *S* wave velocity V_S of 1300 m/s for the first 25 m of depth (retrieved in *Colombero et al.* [2016]), an approximate Rayleigh wave velocity V_R of 1195 m/s was estimated according to the relation of *Sheriff and Geldart* [1982]. Introducing *m*1 and *m*2 cutoff frequencies in equation (1), $z1$ of around 14 m for $F4_1$ and $z2$ of 8 m for $F4_2$ provide a first rough estimate of the fracture open depths. Considering an uncertainty of ±50 m/s in V_R and ±5 Hz in the cutoff frequency reading from the *T/I* curves, average uncertainties of ±4 m for $z1$ and ±2 m for $z2$ are expected.

4.2. Two-Dimensional Numerical Modeling

The continuous-medium finite element software Comsol Multiphysics was used for a quantitative validation of fracture open depths. A 2-D linear elastic model was produced to simulate the real shots in time-domain transient analysis. Large model dimensions were chosen to simulate a half-space configuration. A rectangular model, with a height of 1000 m and a width of 4000 m, was built. To avoid strong wave reflections at the borders of the domain, low-reflecting boundaries were applied at the bottom and lateral sides, and the bottom corner points were fixed to zero displacement. The upper surface was left free; in its central part a synthetic recording array of 48 geophones with 0.75 m spacing was built, coherently with the field one. A Ricker wavelet centered at 50 Hz, well reproducing the spectral content of the field data, was chosen as seismic input for the model. After checking wave propagation in the isotropic medium, a layered model was built, better reproducing the seismic velocity field and the physical and mechanical properties of the rock mass derived from the results of *Colombero et al.* [2016]. Adopted parameters are summarized in Table 1.

Free triangular mesh was built for the whole model, a mesh refinement window of 200×500 m was applied around and below the synthetic array in order to respect for each layer a maximum element size L_{max} [*Mullen and Belytschko*, 1982] of

$$L_{max} = \frac{\lambda_{min}}{10} = \frac{V_{R\ min}}{10\ f_{max}} \qquad (3)$$

The synthetic dispersion curve obtained on the layered model (Figure 7a) is shown in Figure 7b. Differences with respect to the theoretical curve, computed with the Thomson-Haskell approach [*Thomson*, 1950; *Haskell*, 1953], are present at low frequencies due to the incorrect spatial resolution of the survey line, as reported by *O'Neill* [2004]. Nevertheless, model results showed a general acceptable fitting to the theoretical curve and a

Table 1. Summary of the Physical and Mechanical Parameters Adopted in the 2-D and 3-D Numerical Simulations[a]

	V_P (m/s)	V_S (m/s)	V_R (m/s)	v (-)	E (GPa)	ρ (kg/m^3)	L_{max} Mesh (m)	Thickness (m)
				2-D Isotropic Model (And 3-D Models)				
	2700	1500	1379	0.27	14.7	2570	1.3	
				2-D Layered Model				
Layer 1	1250	700	644	0.27	2.99	2400	0.6	2
Layer 2	2000	1100	1011	0.27	7.68	2500	1	8
Layer 3	2700	1500	1379	0.27	5.78	2570	1.3	-

[a]P and S wave velocities (V_P and V_S), Poisson ratios (v), Young's moduli (E), and densities (ρ) are derived from the previous field and laboratory characterization of *Colombero et al.* [2016]. Rayleigh wave velocity (V_R) is retrieved from the V_S-V_R relationship of *Sheriff and Geldart* [1982].

correct match with fracture estimated depths. Using the two cutoff frequencies ($m1$ and $m2$) obtained from prospecting data in equation (1), it is confirmed in Figure 7b that $F4_1$ matches a λ_1 of around 42 m, corresponding to a fracture open depth of 14 m ($z1$), while $F4_2$ corresponds to a λ_2 of approximately 23 m and consequently has a lower estimated depth of around 8 m ($z2$).

The spectral ratio sensitivity to increasing fracture depths was then tested in a layered single- (Figure 7c) and double-fracture (Figure 7e) model, in order to determine for which fracture depths the best fitting between numerical and measured T/I spectral ratios is obtained. Fractures were modeled with a triangular shape, 0.75 m wide on the free surface and coherently reproducing fracture closing with depth.

The single fracture was introduced in the layered model between G28 and G29 (estimated real position for $F4_1$), with a varying depth $z1$ from 2 m to 30 m (Figure 7c). T/I spectral ratios (G30/G27, on the sides of the fracture) are reported in Figure 7d. The model with $z1 = 16$ m shows the smallest offset between the calculated minimum and the measured $m1 = 28$ Hz. Considering the offsets from both minimum and maximum locations, in order to preserve the whole curve shape, the best fitting is found for the model with $z1 = 18$ m. Comparing the numerical results with the rough evaluation proposed in section 4.1 (14 m ± 4 m), $z1$ depth was fixed at 16 m, in an average range between the two estimates.

With this constant $z1$, a second triangular fracture was then introduced between G18 and G19 (estimated real position for $F4_2$), with a depth ($z2$) varying between 2 m and 14 m (Figure 7e), given that the higher cutoff frequency for $F4_2$ suggests a related lower depth. Synthetic T/I spectral ratios related to the double-fracture model are shown in Figure 7f for $F4_1$ (G30/G27) and Figure 7g for $F4_2$ (G20/G17). The model having $z2 = 8$ m (with constant $z1 = 16$ m) is the one showing the minimum offsets from the measured minima and maxima in both plots.

Considering numerical results, we finally accepted a reliable open depth of 16 m ± 2 m for $F4_1$ and 8 m ± 2 m for $F4_2$. These depths and uncertainties are within the range of the rough estimations made on the field spectral ratios at the end of section 4.1.

5. Site Response: Ambient Seismic Noise and Earthquakes

Given the complexity of the reconstructed 3-D fracture setting, passive seismic recordings (ambient noise and earthquakes) are analyzed in this section to investigate the presence of possible resonance frequencies associated to the unstable sectors of the cliff and the fracture control on the related vibration directions.

Different passive seismic monitoring experiments have been performed at the test site in the last years. A temporary survey was carried out by ISTerre-Grenoble during the night between 25 and 26 November 2010, using six triaxial stations (Lennartz LE3-D 5 s, from S1 to S6 in Figure 8) continuously recording for 15 h. Particularly, S1 and S2 were located on the top of the unstable sector A, while S3 and S4 were placed on sector B. The remaining stations (S5 and S6) were installed near the church, in a stable, undisturbed sector of the cliff.

A long-lasting monitoring campaign was later carried out by DST-UNITO, between October 2013 and February 2016, with four 4.5 Hz triaxial geophones (from S7 to S10, in Figure 8). Particularly, S7 was installed at the top of sector A, close to the position of S1 in the previous temporary survey, S8 and S9 were located on
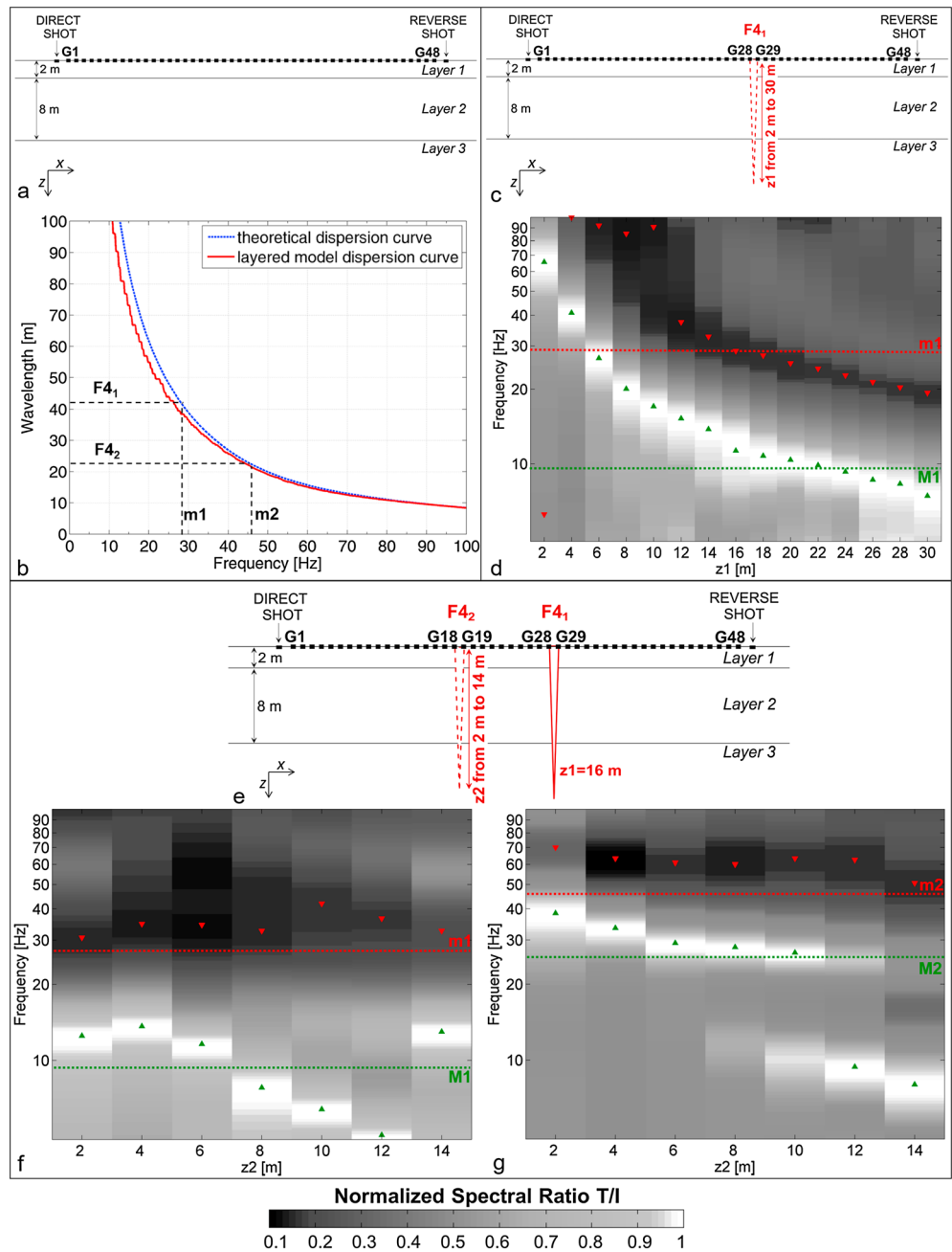
Figure 7. (a) Layered-model configuration, before fracture introduction. (b) Theoretical and synthetic dispersion curves for the layered model. (c) Configuration of the layered model with a single fracture ($F4_1$ between G28 and G29, with depth $z1$ varying from 2 m to 30 m). (d) Normalized T/I spectral ratios (G30/G27) for the layered model in Figure 7c. (e) Configuration of the layered model with two triangular fracture ($F4_1$ between G28 and G29, fixed $z1$ = 16 m; $F4_2$ between G18 and G19, with depth $z2$ varying from 2 m to 14 m). (f) Normalized T/I spectral ratios (G30/G27, across $F4_1$) for the layered model in Figure 7e. (g) Normalized T/I spectral ratios (G20/G17, across $F4_2$) for the layered model in Figure 7e. In Figures 7d, 7f, and 7g, red and green triangles mark the position of minimum and maximum in each modeled spectral ratio. Dashed red and green lines refer to the position of minima (m) and maxima (M), respectively, measured on the field spectral ratios of Figures 6a and 6b.

the southeastern and northern faces of sector A, respectively, at an elevation of around −45 m from the summit of the cliff. Finally, S10 was placed outside the unstable area, west of sector B. Disregarding lacking temporal windows due to system malfunctioning, this second monitoring experience resulted in 8816 h of continuous noise recordings (at a sampling frequency of 250 Hz). During the same period, more than 100
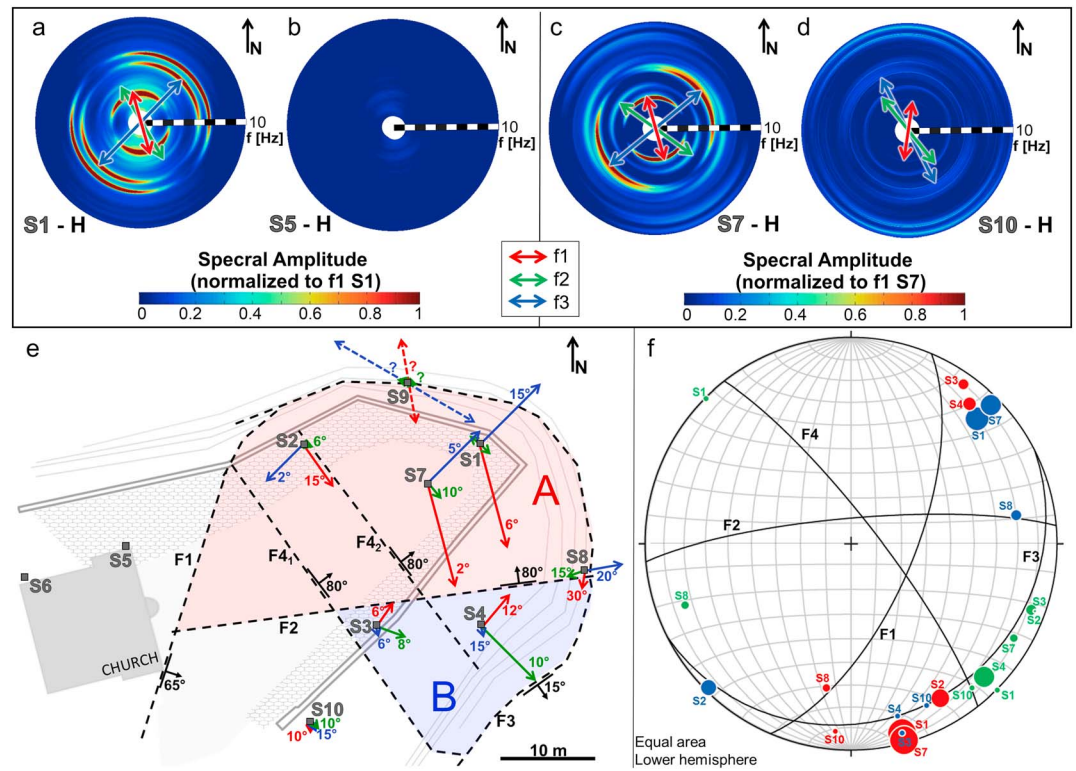
Figure 8. Average spectral polar plots computed in the horizontal plane for (a, b) S1–S5 (temporary survey 2010, ISTerre Grenoble) and (c, d) S7-S10 (DST-UNITO, 2013–2016). The radius of each circle displays frequency (0–10 Hz). (e) Summary of the 3-D orientations for the first three detected resonance frequencies ($f1 = 2.9$ Hz, in red; $f2 = 4$ Hz, in green, and $f3 = 5.5$ Hz, in blue) in planar view. The tip of each arrow marks the dip direction in the vertical plane, while the length is proportional to the spectral amplitude of each detected frequency peak normalized to the amplitude of $f1$ recorded at S1 and S7, for the two passive surveys. The vertical component of S9 was not available for the computation of the dip direction (dashed colored arrows). (f) Stereographic projection of the 3-D vibration orientations compared to fracture orientations, the radius of each circle is proportional to the peak amplitude, normalized to $f1$ value measured at S1 and S7 (for the two different surveys); $f1 = 2.9$ Hz, in red; $f2 = 4$ Hz, in green, and $f3 = 5.5$ Hz, in blue.

local and regional earthquakes were recorded. These events were detected with a STA/LTA (Short Time Average over Long Time Average) algorithm, with LTA- and STA-window lengths of 0.3 s and 30 s, respectively, and a trigger threshold level fixed to 6. Details on the epicenter locations (latitude, longitude), focal depths, and local magnitudes were retrieved for 65 events from the Italian seismological instrumental and parametric database (ISIDe) released by INGV (http://iside.rm.ingv.it/). Extracted earthquakes have distances from the test site varying from 30 km to 570 km, local magnitudes in the range 2.0–4.7 and cover almost all the possible azimuth of provenience to the site (Figure 9a).

Hour-long ambient noise recordings of both the long- (DST-UNITO) and short-term (ISTerre-Grenoble) monitoring campaigns were processed following the procedure introduced by *Bendat and Piersol* [1971] and later modified and tested in several case studies by *McNamara and Buland* [2004]. Resulting Power Spectral Densities (PSDs) were found to coherently fall within the New High and Low Noise Models (NHNM, NLNM) of *Peterson* [1993]. However, the 4.5 Hz permanent geophones (from S7 to S10), with a nominal sensitivity of 44 V/(m/s), demonstrated to be almost insensitive below 2–2.5 Hz. Noise spectral peaks which did not exhibit a variation in time were interpreted as induced by anthropic sources in the surroundings of the cliff. Conversely, spectral peaks manifesting oscillations within the monitored periods were considered as natural frequencies of the site. For the stations located within the unstable sector A, averaging the 8816 hourly results (DST-UNITO), the first three spectral peaks were found to be located around 2.9 Hz ($f1$), 4 Hz ($f2$), and 5.5 Hz ($f3$). Seasonal variations of around ±10% from the average frequency values were detected as a consequence of the air temperature control on the resonance frequencies, as already observed in *Lévy et al.* [2010] and *Bottelin et al.* [2013b]. Fully comparable results in terms of values and amplitude of the frequency peaks
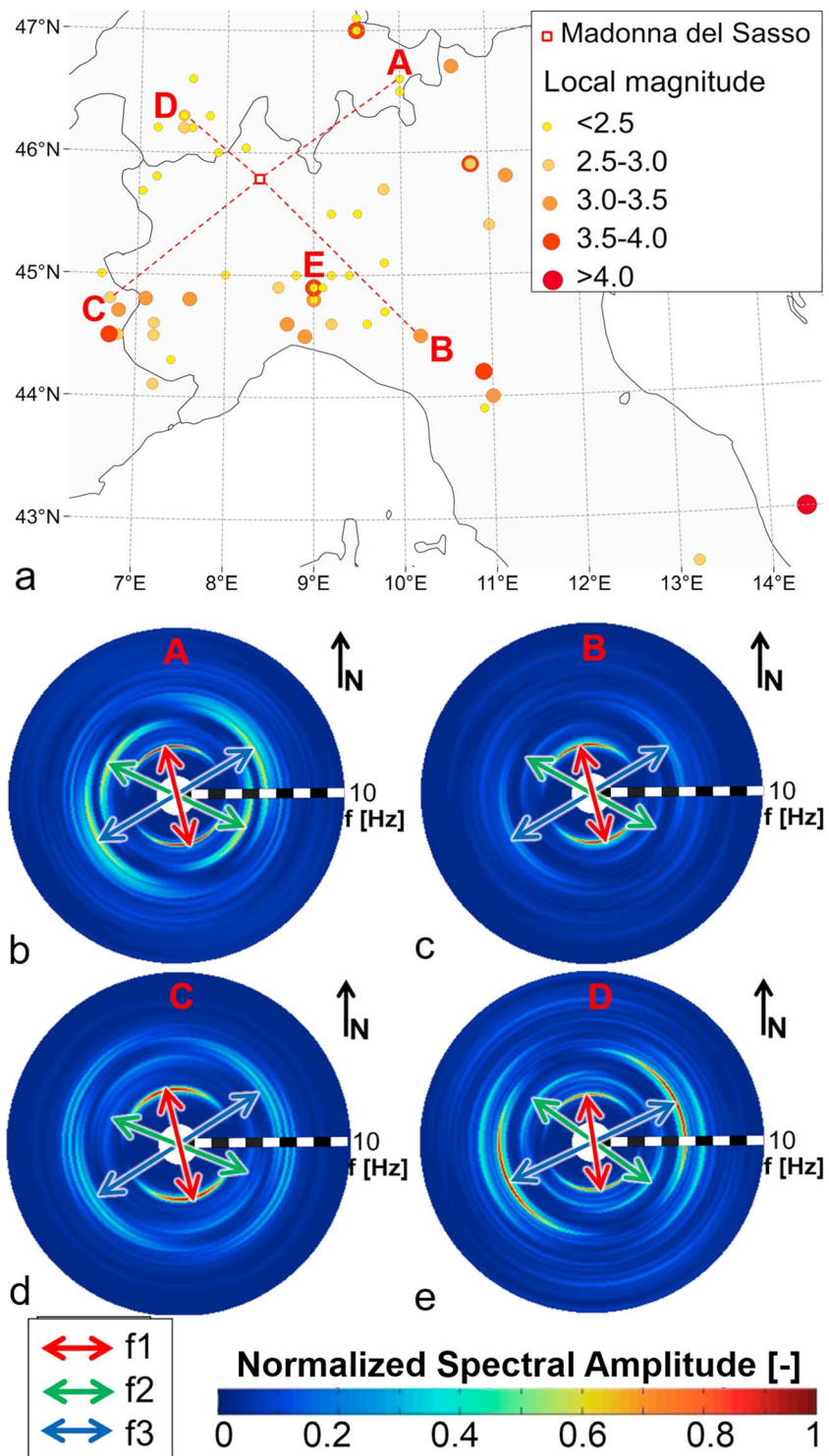
Figure 9. (a) Epicentral location map of 65 earthquakes recorded at the test site. A–D: selection of four events with almost perpendicular azimuthal directions from Madonna del Sasso. A: 27/11/2015, 11:34:59.87, 46.59°N, 9.95°E, depth = 8.4 km, ML = 2.0, distance = 151 km, azimuth = 54°. B: 18/12/2013, 04:00:54.30, 44.52°N, 10.20°E, depth = 24.6 km, ML = 3.4, distance = 201 km, azimuth = 135°. C: 12/06/2014, 11:46:48.39, 44.70°N, 6.78°E, depth = 9.7 km, ML = 3.3, distance = 174 km, azimuth = 225°. D: 14/10/2015, 00:13:45.23, 46.29°N, 7.54°E, depth = 9.8 km, ML = 2.9, distance = 85 km, azimuth = 310°. E: closest event with magnitude >3.5, used for numerical simulations in Figure 11. Horizontal spectral polar plots (radius = frequency, 0–10 Hz) at S7 for (b) event A, (c) event B, (d) event C, and (e) event D. Polar plots are plotted in the same color scale, with spectral amplitude normalized to f1 spectral value at S7. In each plot, frequency values and related vibration directions are highlighted in red for f1, in green for f2, and in red for f3.

Table 2. Comparison Between Average Field (NOISE: Ambient Seismic Noise; EQs: Earthquakes) and Numerical Results for the Orientation of the First Three Resonance Frequencies, at All the Stations Placed at the Top of the Unstable Sectors A and B[a]

				Measured					Calculated	
NOISE	$f1$ = 2.9 Hz $f2$ = 4 Hz $f3$ = 5.5 Hz			Spectral	$f1$ = 2.3 Hz*/2.7 Hz**				Spectral	
		DipDir	Dip	Amplitude	$f2$ = 4.1 Hz*/3.4 Hz**		DipDir	Dip	Amplitude	
EQs	$f1$ = 2.8 Hz $f2$ = 3.9 Hz $f3$ = 5.3 Hz	(° from N)	(deg)	Norm to $f1$(S1)	$f3$ = 6.4 Hz*/5.6 Hz**		(° from N)	(deg)	Norm to $f1$(S1)	
S1	$f1$	165	6	1	S1	$f1$	162	2	1	
	$f2$	135	0	0.15		$f2$	90	1	0.2	
	$f3$	45	15	0.8		$f3$	75	7	0.2	
S2	$f1$	150	15	0.6	S2	$f1$	150	5	0.4	
	$f2$	110	6	0.05		$f2$	110	4	0.3	
	$f3$	225	2	0.5		$f3$	45	1	0.5	
S3	$f1$	35	6	0.3	S3	$f1$	15	5	0.5	
	$f2$	110	8	0.3		$f2$	88	3	0.8	
	$f3$	165	6	0.1		$f3$	155	3	0.2	
S4	$f1$	40	12	0.4	S4	$f1$	15	3	0.7	
	$f2$	135	10	0.7		$f2$	82	1	0.8	
	$f3$	165	15	0.1		$f3$	100	20	0.1	
S7	$f1$ (NOISE)	165	2	1	S7	$f1$	167	2	0.8	
	(EQs)	*165*	*2*	*1*						
	$f2$ (NOISE)	120	10	0.2		$f2$	98	1	0.3	
	(EQs)	*115*	*8*	*0.3*						
	$f3$ (NOISE)	45	5	0.7		$f3$	48	4	0.2	
	(EQs)	*50*	*4*	*0.5*						

[a]Numerical results for *(i) model of sector A and B; **(ii) the whole cliff.

were obtained comparing S1 (ISTerre-Grenoble) and S7 (DST-UNITO) recordings, thus allowing for a reliable merging of the two data sets. No spectral peaks were detected at the stable stations S5 and S6, while S10 exhibited weak amplification around $f1$, $f2$, and $f3$, probably due to its increased proximity to the unstable area. These evidences led to interpret $f1$, $f2$, and $f3$ as the first three resonance frequencies of the site.

Spectral analysis of the recorded earthquakes confirmed the presence of the same first three spectral peaks, with $f1$ = 2.8 Hz, $f2$ = 3.9 Hz, and $f3$ = 5.3 Hz, averaged over 65 events, coherently within the range of seasonal fluctuation detected from the long-term ambient noise analysis.

In order to retrieve the 3-D orientation of the detected spectral peaks, the spectral content of the north-south (N), east-west (E), and vertical (V) components of each station was computed both for noise and earthquakes. Each 1 h noise recording was cut in shorter windows (100 s) tapered with a 10% cosine function. On each 100 s segment the FFT was calculated. The resulting spectra were then smoothed following the technique of *Konno and Omachi* [1998] and averaged over the whole length of the recordings. For earthquakes, windows of variable length, corresponding to 3 times the lag between *P* and *S* wave arrivals of each event, were used for FFT computation. From the composition of the N and E spectra of each station, the frequency distribution (radial axis) and the related azimuth (polar angle) of the vibration energy in the horizontal plane were calculated using an angular increment of 1°. Azimuths were displayed in polar plots, clockwise from N, in the 1–10 Hz range (radial direction of each circle; e.g., Figures 8a–8d for noise recordings; Figures 9b–9d for earthquakes). Similarly, composing the horizontal spectrum obtained along the direction of each frequency peak ($f1$, $f2$, and $f3$) and the spectrum of the V component, the 3-D orientation of the first three natural frequencies detected on each station was obtained. For the unstable compartments, noise spectral polar plots exhibited clear peaks at specific orientations and frequencies (see the average horizontal polar plots of S1 and S7 in Figures 8a and 8c). In contrast, null (S5, Figure 8b) or less significant (S10, Figure 8d) peaks in amplitude and directionality were observed on the plots for the stable sector. A summary of the 3-D orientations and spectral amplitudes obtained from ambient noise analysis for $f1$, $f2$, and $f3$ at all the considered stations (reported in Table 2) is shown in simplified planar view (Figure 8e) and stereographic projection (Figure 8f) for direct comparison with fracture orientations.

The interpretation of these data is not straightforward as for the cited nearly 2-D case studies, in which the vibration motion at the first resonance frequency ($f1$) was systematically found to have the highest spectral amplitude and to be oriented perpendicularly to the main fracture set separating the unstable and stable

sectors [e.g., *Lévy et al.,* 2010; *Burjánek et al.,* 2012; *Del Gaudio et al.,* 2013; *Bottelin et al.,* 2013a]. The vibration directions are here complicated by the presence of two distinct unstable blocks, which are separated by a complex 3-D fracture setting and constrained to a sloping basal discontinuity. Each monitoring station seems to be mostly influenced by the orientation of the closest fracture (Figure 8e). When a station is placed between two fractures, at a similar distance (e.g., S3, between $F4_1$ and F2), the coupled control of both structural orientations is observed. Focusing on sector A, the greatest peaks are found for $f1$ and close to the cliff edge (S1 and S7) with a nearly N-S vibration direction, dipping according to the basal fracture F3 (Figure 8f). Conversely, on sector B, $f1$ is not systematically the strongest spectral peak ($f2$ is predominant on S4, Figure 8e) and the related dip directions do not follow the basal constraint (Figure 8f). Comparing $f1$ and fracture orientations on the horizontal plane for the unstable sector A, at S2 the vibration direction is perfectly aligned with the strike of the closest fracture $F4_2$. On the east of this discontinuity, an additional influence of F2 seems to control $f1$ orientations at S1 and S7, with $f1$ peaks oriented almost perpendicular to this fracture. The second spectral peak $f2$ shows higher amplitudes on sector B, where it is almost perpendicular to the first-mode $f1$, differently from sector A. Particularly, $f2$ vibration is almost perpendicular to $F2$-$F4_1$ intersection at S3, and to $F4_2$ at S4. Weak spectral peaks are found at $f2$ on sector A, with an orientation almost parallel to $F4_1$ and $F4_2$ at S1 and S7 and similar to S3 at S2. All the $f2$ dips are inclined according to the basal fracture F3. Conversely, $f3$ is stronger on sector A, with spectral amplitudes comparable to $f1$. On sector A, orientations are almost perpendicular to fractures $F4_1$ and $F4_2$, with opposite dips on the two sides of $F4_2$. The weak $f3$ peaks recorded on sector B are almost perpendicular to F2.

All the considered earthquakes (Figure 9a) exhibited spatial orientations (average directions for $f1$, $f2$, and $f3$ at S7 are reported in Table 2), confirming the results of seismic noise analysis. Angular fluctuations minor than 5° were observed in the horizontal plane for $f1$ vibration direction, thus confirming no influence of the earthquake source azimuth in the resonance frequency orientations, as shown in Figures 9b–9e for four different events with almost perpendicular azimuth of provenience to the test site. This underlined the site-dependent nature of these three spectral peaks and additionally validated their interpretation as resonance frequencies of the unstable cliff, with orientations controlled by the 3-D structural setting of the site.

6. The 3-D Numerical Modeling

The 3-D modeling of the cliff response was undertaken in order to combine the results of field observations, noncontact geomechanical survey, active and passive seismic data, for a final interpretation of the 3-D fracture control on the site stability. Numerical modeling was essential to confirm quantitatively that the obtained 3-D fracture setting is the cause of the complex resonance frequency orientations detected from the passive surveys and to retrieve the associated vibration modes.

6.1. The 3-D Model Construction

A simplified geometry of the cliff was built in Comsol Multiphysics environment; volumes for sectors A and B were reproduced simplifying the DSM obtained from the laser scanning and photogrammetric surveys. Georeferenced field and noncontact observations were used to locate fracture intersections with the face topography. Fractures were introduced as planar surfaces, extrapolating plane equations from the average fracture orientations (Figure 3). An opening of 0.75 m was considered reliable for the $F4_1$, $F4_2$, and F2, according to field observations at the top of the cliff and results from 2-D numerical modeling. From the latter, $F4_1$ and $F4_2$ open depths were fixed to 16 m and 8 m, respectively.

Different attempts were made to constrain F2 depth. Field observations suggested an open depth of at least 10 m in the open chasm observable at the eastern edge of the cliff. The 3-D modeling results were found to be closer to field data with a F2 fracture depth minor or equal to $F4_1$ depth. For greater depths, $f1$ and $f3$ peaks showed the highest spectral amplitudes on sector B, not coherently with noise field results. Therefore, an open depth of 16 m both for F2 and $F4_1$ was considered, giving the best fitting with the real measurements.

The final average height of the modeled unstable cliff is 44 m. The calculated total unstable volume is 12,300 m^3. Particularly, the volumes related to sector A and B are 6000 m^3 and 6300 m^3, respectively. Automatic meshing with tetrahedral finite elements was applied on the model geometry. Two different simulations were performed considering the following:
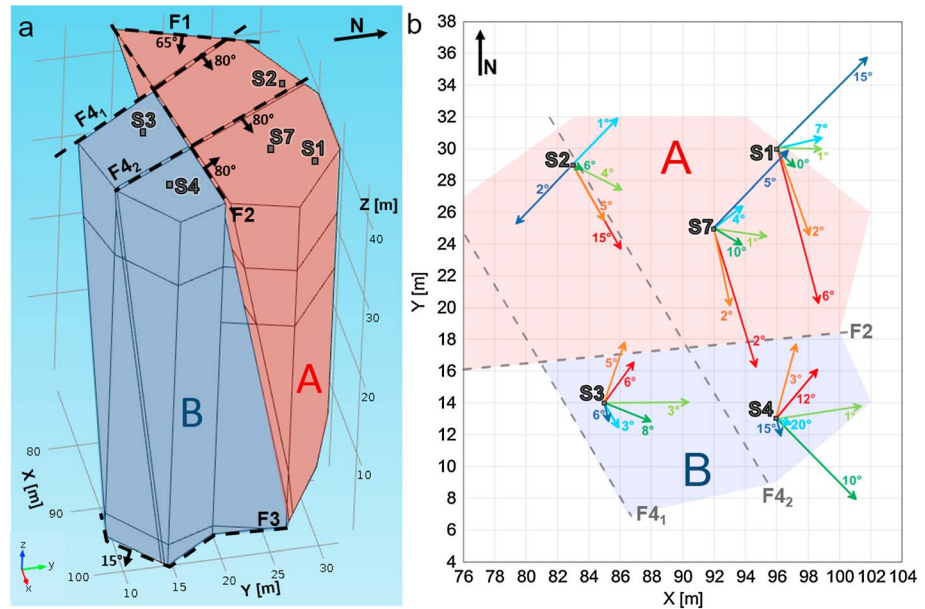
Figure 10. (a) A 3-D model of sector A and sector B with fracture orientations. (b) Comparison of the field and synthetic orientations for the first three resonance frequencies in a planar view. The tip of the arrows marks the dip direction in the vertical plane (with dip indication). The length of the arrows is proportional to the spectral amplitude (for field data) and to the total displacement (for modeling results) normalized to f1 spectral value at S1 and S7, for each passive survey.

1. Only the unstable volumes (sectors A and B, Figure 10a); in this case the boundaries to the stable sector were simulated introducing spring coupling along F1 (back of sector A), F2 (back of sector B, beyond 16 m), and F3 (at the base). All the other surfaces were left free to move.
2. Unstable volumes (sectors A and B) connected to a simplified model of the stable cliff (Figure 12); in this case thin elastic layers were introduced between the stable and unstable parts, and boundaries of the stable parts were fixed to zero displacement, while all the other faces were left free.

This double check was necessary to test that resonant frequencies resulting from simulations are not affected by the mass of the stable sector and are related only to the unstable sectors of the cliff. Moreover, modeling only the unstable portion of the cliff did not allow for testing the response at the stations placed outside the unstable domain (S5, S6, and S10). Adopted physicomechanical properties were taken from the 2-D isotropic model (Table 1), disregarding the shallow low-velocity layers, in order to simplify mesh refinement and speed computations.

6.2. Passive Seismic Data and Model Validation

In order to validate the noise field measurements in terms of resonance frequency values and 3-D orientations as a function of the reconstructed fracture conditions, a modal eigenfrequency study was performed at the location of all the stations placed at the summit of the unstable volumes (S1–S4 and S7, Figure 10a). The two tested models (i and ii) gave fully comparable results in terms of motion orientations, with a slight difference (<5%) in the values obtained for the first three resonance frequencies. Average results are plotted in a planar view in Figure 10b and summarized in Table 2, for direct comparison with field noise measurements.

To further confirm the model validity, the propagation throughout the unstable sectors of natural earthquakes recorded at the site was tested. Earthquake waveforms recorded at S8 were used as seismic input at the base of the unstable sectors, to model the propagation and response at the top of the column. This was achieved comparing field and synthetic results of S7, at the top of the unstable sector A, and S10, located just outside the unstable area. Earthquake records were introduced as measured velocity on each spatial component (N8, E8, V8), after tapering with a 10% cosine window. A time-dependent study was then performed, to generate synthetic seismograms for the three components of S7 and S10. Synthetic waveforms were processed as the real ones to compute resonance frequencies and related spatial orientations. An
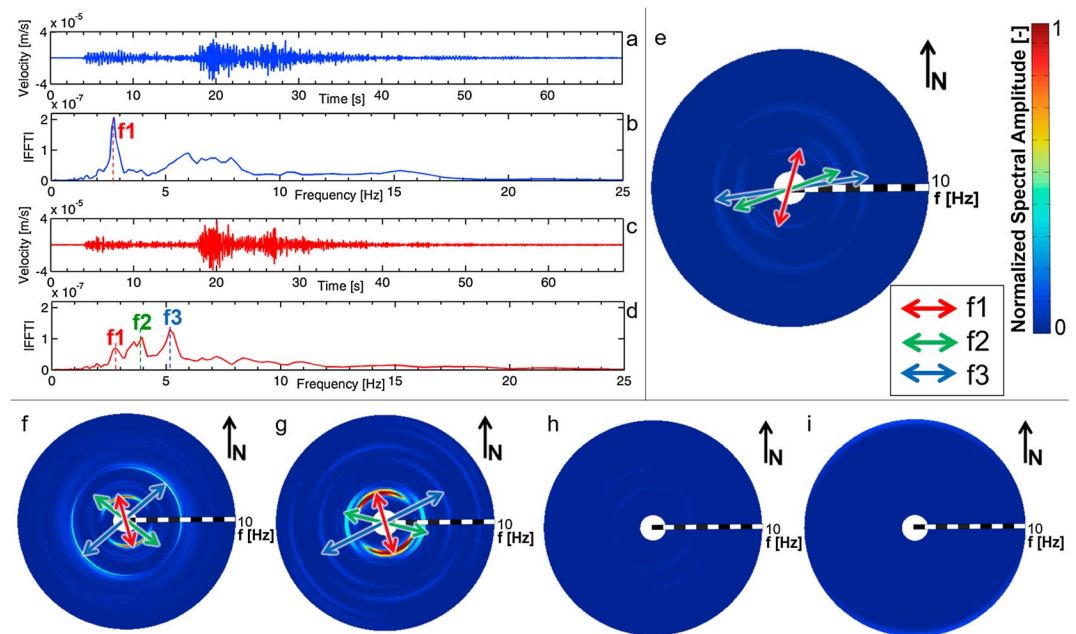
Figure 11. Numerical simulations using a real earthquake (21/11/2013, 10:34:15.33, 44.92°N, 9.05°E, depth = 18.9 km, ML = 3.1, distance = 110 km; location is shown with E in Figure 10a). (a) N8 seismogram, (b) N8 Fourier spectrum, (c) E8 seismogram, (d) E8 Fourier spectrum. (e) S8 measured polar plot on the horizontal plane (obtained from Figures 11b and 11d). (f) S7 measured polar plot for the same event. (g) S7 numerical polar plot (from the synthetic seismograms obtained using the event as seismic input in the 3-D model at S8 location). (h) S10 measured polar plot for the same event. (i) S10 numerical polar plot (from the synthetic seismograms obtained using the event as seismic input in the 3-D model at S8 location). Polar plots (radius = frequency, 0–10 Hz) are plotted in the same color scale, with spectral amplitude normalized to f1 spectral value at S7.

example of simulation, using the earthquake with a local magnitude >3.5 closer to the site (E in Figure 9a), is shown in Figure 11. N8 and E8 field recordings are shown (Figures 11a and 11c), together with the related Fourier spectra (Figures 11b and 11d). In the resulting S8 horizontal spectral plot (Figure 11e) the event exhibits three first spectral peaks located around 2.7, 3.8, and 5.2 Hz. These frequency values are slightly lower than the average ones computed over the whole earthquake data set, since the example event was recorded in late November, when the values of the resonance frequencies of the unstable volume decrease, according to a decrease in the air temperature value. Modeling results and field data are compared in the polar plots of Figure 11 (Figures 11f and 11h show the real data for S7 and S10, respectively, Figures 11g and 11i) are the numerical results related to the same stations). The first three resonance frequencies obtained from the modeling at S7 (Figure 11g) are centered around 2.8, 3.7, and 5.9 Hz, coherently matching the measured values (Figure 11f). The orientations of real and synthetic data perfectly match for f1 and f3, while about 15° of divergence are present for f2 orientation. The simulated f2 shows a spectral amplitude higher than f3, differently from field results. On the stable S10, which exhibited weak spectral peaks (Figure 11h) maybe due to its close position to the unstable area, numerical simulations confirm the total absence of significant resonance frequencies (Figure 11i). Despite the uncertainties and approximations on many input parameters (e.g., the real geometry of the fractures, the heterogeneities in the physical and mechanical parameters), numerical results are close in value and orientation to field measurements, thus globally validating the reconstructed 3-D fracture geometry of the cliff adopted for the model and furnishing a quantitative help in the interpretation of the site observations.

6.3. Vibration Mode Interpretation

The 3-D displacements fields reconstructed from the eigenfrequency analysis, showing the complete vibration modes at the first three resonance frequencies, are reported in Figure 12. The first mode (f1, in Figures 12a and 12b) is dominated by bending almost perpendicular to F2 and parallel to F4$_1$ on sector A. Since the two fractures are not perpendicular, a superimposed weaker torsional component is present,
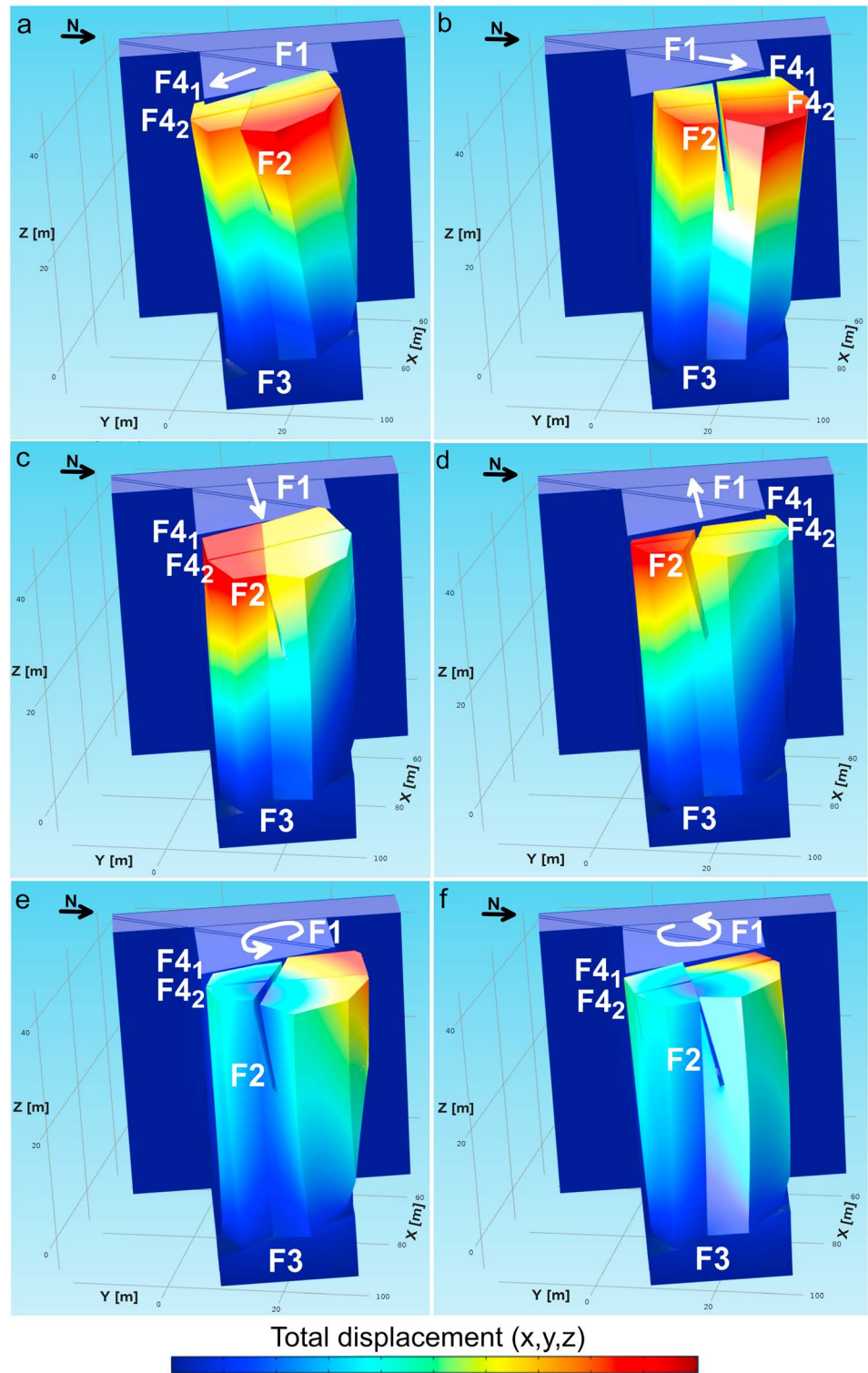
Figure 12. Results of modal analysis on the complete 3-D model for the first three vibration modes: (a, b) *f*1, (c, d) *f*2, and (e, f) *f*3.

centered almost around the F2-F4$_1$ intersection. A different behavior on the two sides of F4$_2$ is also detected, coherently with field measurements. Particularly, a deviation of 15° is observed in the horizontal plane between S2 and the stations closer to the cliff edge (S1 and S7) both for measured and calculated data (Figure 10b). Actually, S2 is located to the west of F4$_2$ and shows a first vibration mode dipping parallel to F4$_1$ and matching the dip of the basal F3. To the east of F4$_2$, S1 and S7 show lower dip with an increased dip direction from north, maybe due to a major effect of the open fracture F2 in this area. Sector B exhibits $f1$ inclination opposite to the basal F3, both in real and synthetic data, with $f1$ orientation mainly perpendicular to the intersection between F2 and F4$_2$, which are both close to the stations. The second vibration mode ($f2$, in Figures 12c and 12d) is more evident on sector B, in agreement with field measurements, and dominated by bending almost parallel to F2, or perpendicular to F4$_1$. While field data showed a combined effect of both F4$_2$ and F2 on $f2$ orientations on sector B, numerical results are almost purely parallel to F2. Lower angular deviations are present on sector A. The third vibration mode ($f3$, in Figures 12e and 12f) is driven by torsion around the vertical axis passing through the F2-F4$_1$ intersection, and it shows higher displacements on sector A, coherently with field data. Nevertheless, even if field and numerical orientations at S2 are perfectly matching on the horizontal plane, the dip direction is opposite (Figure 10b).

7. Conclusions

In this work, noncontact geomechanical measurements and active/passive seismic surveys are combined into a multimethodological approach for the characterization of the complex 3-D fracture setting of an unstable cliff, in order to overcome survey limitations imposed by the inaccessible steep topography and site morphology. All the acquired data were devoted to the construction of a fully 3-D numerical model of the cliff. The combined analysis of field measurements and numerical modeling has given important insights into the mechanical behavior and response of the rock mass to its peculiar structural settings.

A detailed Digital Surface Model of the site, resulting from a previous ground-based laser-scanning and photogrammetric survey of the cliff, supplied the geometrical bases for identifying fracture locations and orientations on the otherwise unattainable rock exposures. The location of the main fractures was validated throughout an active seismic line acquired at the top of the cliff. Furthermore, surface wave analysis on the prospecting data revealed to be a powerful tool to constrain the depth of the investigated fractures. Particularly, two of the main fractures isolating the unstable volumes were estimated to have an approximate open depth of 14 m ± 4 m and 8 m ± 2 m. Fracture persistence was also constrained by 2-D numerical simulations reproducing seismic wave propagation in the fractured medium, which resulted into a final estimation of 16 m ± 2 m and 8 m ± 2 m for two fracture depths. The defined fracture geometry at the site provided a reliable essential basis for the 3-D modeling of the site response.

Long- and short-term ambient seismic noise recordings were further used to understand the control of fracture geometry on the dynamic behavior of the unstable cliff. On the recordings of the stations located within the unstable sectors, noise spectral analysis revealed the presence of three clear spectral peaks, affected by frequency fluctuations (±10% from the average value in a seasonal cycle) linked to air temperature variations. No comparable spectral amplification was found within the stable areas. Spectral analysis of earthquakes recorded within the same monitored period confirmed the presence of the same first three spectral peaks, with frequency values within the range of the seasonal fluctuations detected from ambient seismic noise and orientations independent from the azimuth of the earthquake source. On these bases, these frequencies were interpreted as the first three resonance frequencies of the site.

Noise-earthquake comparison showed that the presence of resonance phenomena within the unstable sectors can be determined from both seismic data sets. Long-term ambient noise monitoring has, however, the added value to follow the fluctuations of the resonance frequencies with time. Since abrupt falls in the resonance frequency values may reflect a change in the stiffness of the constraints of the unstable sectors, failure precursors can be potentially highlighted with long-term noise monitoring campaigns.

The 3-D orientation of the three resonance frequencies showed strong variability between the two unstable sectors, with vibration directions controlled by the fractures closest to each station. The open subvertical fractures revealed the strongest constraint to the frequency dip directions, while the sloping basal fracture was found to control the majority of the dip angles.

These complex results highlighted the difference between the nearly 2-D geometry of previous literature studies, characterized by an unstable volume separated from the stable rock mass by a single planar fracture [e.g., *Lévy et al.,* 2010; *Bottelin et al.,* 2013b; *Valentin et al.,* 2017], and the fully 3-D complex setting of discontinuities of Madonna del Sasso. Thus, 3-D FEM modeling became a necessary support to the study. Despite minor discrepancies between field and numerical results, which can be considered intrinsic of the uncertainties in the model input parameters (i.e., fracture geometry approximated to planar surfaces with a constant arbitrary lateral opening for the whole length, local heterogeneities in the physical and mechanical parameters not taken into account), 3-D modeling simultaneously allowed for

1. validation of the 3-D fracture geometry of the cliff reconstructed from surface and active seismic investigations;
2. reproducibility of the field passive seismic measurements in terms of frequency values and orientations with satisfactory accuracy, which is an added value considering the complexity of the case study and the absence of reference works in fully 3-D fractured sites; and
3. interpretation of the first three vibration modes of the studied cliff as a function of its peculiar fracturing state.

In agreement with *Bottelin et al.* [2013b] on a simpler nearly 2-D case study, the modeling results highlighted that the first two detected vibration modes are mainly related to bending roughly perpendicular and parallel to the cliff elongation, while the third mode is dominated by torsion. However, the presence of several intersecting fractures and two separated compartments complicates the site response, resulting in different vibration amplitudes and orientations on the two unstable sectors.

A complete comprehension of the fracture-driven dynamic behavior of the unstable rock mass was possible only with the integration of the different methodologies presented within this work. Particularly, the approach provided consistent information on the fracture depth and on the internal fracturing of the prone-to-fall mass, which are key parameters for rock stability assessment. In addition, it strengthened the value of ambient seismic noise studies for determining the resonance properties of an unstable rock volume decoupling from the massif, even in complex 3-D fracture settings, and thus offering relevant perspectives to monitor possible evolutions toward the final collapse.

References

Bendat, J. S., and A. G. Piersol (1971), *Random Data: Analysis and Measurement Procedures*, 407 pp., Wiley, New York.

Bergamo, P., and L. V. Socco (2014), Detection of sharp later discontinuities through the analysis of surface-wave propagation, *Geophysics*, *79*(4), EN77–EN90.

Bièvre, G., D. Jongmans, T. Winiarski, and V. Zumbo (2012), Application of geophysical measurements for assessing the role of fissures in water infiltration within a clay landslide (Trieves area, French alps), *Hydrol. Processes*, *26*, 2128–2142.

Bistacchi, A., W. A. Griffith, S. A. F. Smith, G. Di Toro, R. Jones, and S. Nielsen (2011), Fault roughness at seismogenic depths from LIDAR and photogrammetric analysis, *Pure Appl. Geophys.*, *168*(12), 2345–2363.

Boriani, A., and E. Giobbi (2004), Does the basement of western alps display a tilted section through the continental crust? A review and discussion, *Per. Mineral.*, *73*(2), 5–22.

Bottelin, P., C. Lévy, L. Baillet, D. Jongmans, and P. Gueguen (2013a), Modal and thermal analysis of Les Arches unstable rock column (Vercors massif, French Alps), *Geophys. J. Int.*, *194*, 849–858.

Bottelin, P., et al. (2013b), Spectral analysis of prone-to-fall rock compartments using ambient vibrations, *J. Environ. Eng. Geophys.*, *18*, 205–217.

Bottelin, P., J. Valentin, D. Jongmans, L. Baillet, F. Donze, O. Brenguier and A. Mangeney (2015), Role of fracturing on seismic noise measurements—The case study of the Bory crater (La Réunion Island), in *Proceedings of the Near Surface Geoscience 2015 —21st European Meeting of Environmental and Engineering Geophysics*, pp. 1–4, Turin, Italy, 6–10 Sept.

Burjánek, J., J. R. Moore, G. Grassner-Stamm, and D. Fäh (2012), Instrumental evidence of normal mode rock slope vibration, *Geophys. J. Int.*, *188*, 559–569.

Coggan, J. S., A. Wetherelt, X. P. Gwynn, and Z. Flynn (2007), Comparison of hand-mapping with remote data capture systems for effective rock mass characterization, in *Proceedings of 11th Congress of the International Society for Rock Mechanics—The Second Half Century of Rock Mechanics*, vol. 1, pp. 201–205, Taylor & Francis Group, London.

Colombero, C., C. Comina, G. Umili, and S. Vinciguerra (2016), Multiscale geophysical characterization of an unstable rock mass, *Tectonophysics*, *675*, 275–289, doi:10.1016/j.tecto.2016.02.045.

De Souza, M. K., F. M. Veronez, W. Tognoli Jr., L. G. Da Silveira, L. C. Inociencio, R. M. Da Silva, and R. C. C. Modena (2013), Terrestrial laser scanning: Application for measuring of structures information in geological outcrops, *Int. J. Adv. Remote Sens. GIS*, *2*(1), 260–270.

Del Gaudio, V., S. Muscillo, and J. Wasowski (2013), New developments in the use of ambient noise analysis to characterise the seismic response of landslide prone slopes, *Nat. Hazards Earth Syst. Sci.*, *13*, 2075–2087, doi:10.5194/nhess-13-2075-2013.

Ferrero, A. M., G. Forlani, R. Rondella, and H. I. Voyat (2009), Advanced geostructural survey methods applied to rock mass characterization, *Rock Mech. Rock. Eng.*, *42*(4), 631–665.

Frayssines, M., and D. Hantz (2006), Failure mechanisms and triggering factors in calcareous cliffs of the subalpine ranges (French Alps), *Eng. Geol.*, *86*(4), 256–270.

Haskell, N. A. (1953), The dispersion of surface waves from point sources in a multi-layered medium, *Bull. Seismol. Soc. Am.*, *54*, 377–393.

Heincke, B., H. Maurer, A. G. Green, H. Willenberg, T. Spillmann, and L. Burlini (2006), Characterizing an unstable mountain slope using shallow 2-D and 3-D seismic tomography, *Geophysics*, *71*(6), B241–B256.

Hévin, G., O. Abraham, H. A. Pedersen, and M. Campillo (1998), Characterisation of surface cracks with Rayleigh waves: A numerical model, *NDT E Int.*, *31*(4), 289–297.

Hyslop, C., and R. Stewart (2015), Imaging lateral heterogeneity using reflected surface waves, *Geophysics*, *80*(3), EN69–EN82.

Jongmans, D., P. Hemroulle, D. Demanet, F. Renardy, and Y. Vanbrabant (2000), Application of 2-D electrical and seismic tomography techniques for investigating landslides, *Eur. J. Environ. Eng. Geophys.*, *8*, 75–89.

Konno, K., and T. Omachi (1998), Ground-motion characteristics estimated from spectral ratio between horizontal and vertical components of microtremor, *Bull. Seismol. Soc. Am.*, *88*(1), 228–241.

Lancellotta, R., P. Gigli and C. Pepe (1991), Relazione tecnica riguardante la caratterizzazione geologico-strutturale dell'ammasso roccioso e le condizioni di stabilità della rupe, commissionata dal Ministero dei Lavori Pubblici - Provveditorato alle Opere Pubbliche per il Piemonte e la Valle d'Aosta, private communication.

Larose, E., et al. (2015), Environmental seismology: What can we learn on Earth surface processes with ambient noise?, *J. Appl. Geophys.*, *116*, 62–74.

Levshin, A. L., T. B. Yanovskaya, A. V. Lander, B. G. Bukchin, M. P. Barmin, L. I. Ratnikova, and E. N. Its (1989), *Seismic Surface Waves in Laterally Inhomogeneous Earth*, edited by V. I. Keilis-Borok, pp. 1–21, Kluwer Publ. House, Dordrecht, Boston, London.

Lévy, C., L. Baillet, D. Jongmans, P. Mourot, and D. Hantz (2010), Dynamic response of the Chamousset rock column (western alps, France), *J. Geophys. Res.*, *115*, F04043, doi:10.1029/2009JF001606.

Li, Y. G., and J. E. Vidale (1996), Low-velocity fault zone guided waves: Numerical investigations of trapping efficiency, *Bull. Seismol. Soc. Am.*, *86*, 371–378.

Mauritsch, J. H., W. Seiberl, R. Arndt, A. Römer, K. Schneiderbauer, and G. P. Sendlhofer (2000), Geophysical investigations of large landslides in the Carnic Region of southern Austria, *Eng. Geol.*, *56*, 373–388.

McNamara, D. E., and R. P. Buland (2004), Ambient noise levels in the continental United States, *Bull. Seismol. Soc. Am.*, *94*(4), 1517–1527.

Méric, O., S. Garambois, D. Jongmans, M. Wathelet, J.-L. Chatelain, and J.-M. Vengeon (2005), Application of geophysical methods for the investigation of the large gravitational mass movement of Séchilienne, France, *Can. Geotech. J.*, *42*, 1105–1115.

Moore, J. R., M. S. Thorne, K. D. Koper, J. R. Wood, K. Goddard, R. Burlacu, S. Doyle, E. Stanfield, and B. White (2016), Anthropogenic sources stimulate resonance of a natural rock bridge, *Geophys. Res. Lett.*, *43*, 9669–9676, doi:10.1002/2016GL070088.

Moore, J. R., V. Gischig, J. Burjánek, S. Loew, and D. Fäh (2011), Site effects in unstable rock slopes: Dynamic behavior of the Randa instability (Switzerland), *Bull. Seismol. Soc. Am.*, *101*, 3110–3116.

Mullen, R., and T. Belytschko (1982), Dispersion analysis of finite element semidiscretizations of the two-dimensional wave equation, *Int. J. Numer. Methods Eng.*, *18*, 11–29.

O'Neill, A. (2004), Shear velocity model appraisal in shallow surface wave inversion, in *Geotechnical and Geophysical Site Characterization*, edited by A. Viana da Fonseca and P. W. Mayne, pp. 539–546, Millpress, Amsterdam.

Peterson, J. (1993), Observations and modelling of background seismic noise, *U.S. Geol. Surv. Open File Rep., 93-322*, 95 pp., Albuquerque, New Mexico.

Salvini, R., M. Francioni, S. Riccucci, F. Bonciani, and I. Callegari (2013), Photogrammetry and laser scanning for analyzing slope stability and rock fall runout along the Domodossola-Iselle railway, the Italian alps, *Geomorphology*, *185*, 110–122.

Sheriff, R. E., and L. P. Geldart (1982), *Exploration Seismology*, *History, Theory and Data Acquisition*, vol. 1, Cambridge Univ. Press, Cambridge.

Sturzenegger, M., and D. Stead (2009), Quantifying discontinuity orientation and persistence on high mountain rock slopes and large landslides using terrestrial remote sensing techniques, *Nat. Hazards Earth Syst. Sci.*, *9*, 267–287.

Thomson, W. T. (1950), Transmission of elastic waves through a stratified solid medium, *J. Appl. Phys.*, *21*, 89–93.

Valentin, J., A. Capron, D. Jongmans, L. Baillet, P. Bottelin, F. Donze, E. Larose, and A. Mangeney (2017), The dynamic response of prone-to-fall columns to ambient vibrations: Comparison between measurements and numerical modelling, *Geophys. J. Int.*, *208*(2), 1058–1076.